M2LW-24OR0402023

Light Water Reactor Sustainability Program

Initial Steps Toward Mitigation of Irradiation Assisted Stress Corrosion Cracking in Stainless Steels

Adam Eichhorn, Gokul Subramanian, Stephen S. Raiman
University of Michigan

September 2024

U.S. Department of Energy
Office of Nuclear Energy

M2LW-24OR0402023

Initial Steps Toward Mitigation of Irradiation Assisted Stress Corrosion Cracking in Stainless Steels

Adam Eichhorn
Gokul Subramanian
Stephen Raiman
University of Michigan

September 2024

Light Water Reactor Sustainability
Materials Research Pathway

http://lwrs.inl.gov

Prepared for the
U.S. Department of Energy
Office of Nuclear Energy

Page intentionally left blank

Summary

With a solid understanding of Irradiation Assisted Stress Corrosion Cracking (IASCC) mechanisms in place, current efforts have turned to mitigation. Three stainless steels with engineered microstructures hypothesized to resist IASCC were chosen for testing: Oxide Dispersion-Strengthened (ODS) 304L, ultrafine-grained (UFG) 304L, and Additively Manufactured and Hot Isostatic Pressed (AM-HIP) 316L. Each material is believed to resist dislocation channeling, a key driver of IASCC. To facilitate the testing of these new materials, a new testing paradigm is being designed and qualified in which samples are irradiated with protons and subjected to 4-point-bend IASCC testing in Pressurized Water Reactor (PWR) conditions. Within this work, the ODS and AM-HIP steels were irradiated to 5 dpa along with wrought 304L stainless steel, while the UFG material is planned for future irradiation. The samples are being prepared for IASCC testing and are currently undergoing post-irradiation examination. New methods for determining the samples' mechanical properties to inform a Finite Element Analysis (FEA) model are discussed, along with the initial results of the characterization.

Acknowledgments

This work was supported by the US Department of Energy, Office of Nuclear Energy, Light Water Reactor Sustainability Program, Materials Research Pathway. The authors acknowledge technical support from the Michigan Center for Materials Characterization, the Michigan Ion Beam Laboratory, and experimental support from Connor Shamberger.

CONTENTS

Summary iii

Acknowledgments iv

Acronyms vi

1. Introduction 1
   - 1.1 Motivation 1
   - 1.2 Background 1
   - 1.3 Approach 2

2. Experiment 4
   - 2.1 Sample Preparation 4
     - 2.1.1 Sample History 4
     - 2.1.2 Four-Point Bend Test Geometry 4
   - 2.2 Irradiation 5
     - 2.2.1 SRIM 5
     - 2.2.2 Stage Preparation 6
   - 2.3 Indentation 6
   - 2.4 IASCC Testing 8
     - 2.4.1 Irradiated Material System 8
     - 2.4.2 Four-Point Bend Fixture 9
     - 2.4.3 IASCC Experimental Setup 10
   - 2.5 Modeling 10
     - 2.5.1 Finite Element Analysis 10

3. Results 11
   - 3.1 Irradiation 11
   - 3.2 Indentation Results 12
   - 3.3 TEM Characterization 13

4. Conclusions 15

5. References 16

Acronyms

4PB	4-Point Bend
AM-HIP	Additively Manufacted and Hot Isostatic Pressed
BSE	Backscatter Electrons
CAD	Computer-Aided Design
DC	Dislocation Channel
EBSD	Electron Backscatter Diffraction
FEA	Finite Element Analysis
FIB	Focused Ion Beam
GB	Grain Boundary
IASCC	Irradiation-Assisted Stress Corrosion Cracking
IM	Irradiated Materials System
IMTL	Irradiated Materials Testing Laboratory
IR	Infrared
LWR	Light Water Reactor
ODS	Oxide-Dispersion Strengthened
PWR	Pressurized Water Reactor
SEM	Scanning Electron Microscope
SRIM	Scanning Range of Ions in Matter
SS	Stainless Steel
TEM	Transmission Electron Microscope
UFG	Ultrafine-Grained
WR	Wrought

1. Introduction

1.1 Motivation

Irradiation-assisted stress corrosion cracking of in-core stainless steel components is a critical issue facing Light Water Reactor (LWR) life extension efforts. As components accrue radiation damage, experience tensile stresses, and are exposed to high-temperature water, intergranular cracks form and propagate in the material. The behavior of core-facing components is critical to economic reactor operation, necessitating a thorough investigation into the mechanisms of IASCC and how it can be mitigated.

1.2 Background

A critical component of IASCC is the formation of dislocation channels. Dislocation channeling is the process by which dislocations in fcc, bcc, and hcp materials clear defects as they move through a slip plane, creating a path from grain boundary to grain boundary for further dislocation motion. Hashimoto et al. [1] showed that high temperature (330 °C) and loss of work hardening are precursors for dislocation channel formation. Dislocation channeling is observed in irradiated materials as a component of irradiation embrittlement caused by nanoscale irradiation defects. As the first dislocations travel on a slip plane to reach the grain boundary, defect clusters are sheared, and work hardening in the channel becomes negligible. McMurtrey et al. showed that slip channels that terminated at grain boundaries were more likely to cause grain boundary cracking, represented in Fig. 1 [2]. It was later shown experimentally by Johnston et al. [3] and computationally by Kuhr et al. [4] that there was a local stress buildup where the dislocations terminated at the grain boundaries but less so when slip channels continued through grain boundaries.

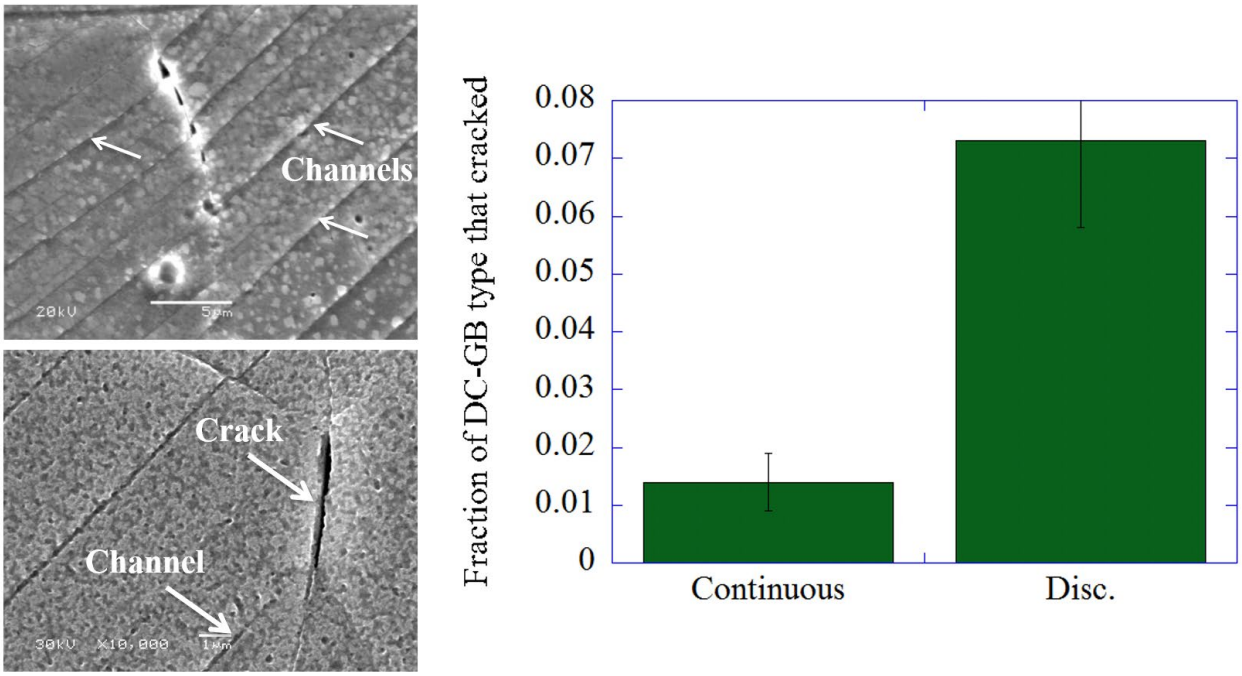

Figure 1: Images of continuous and discontinuous dislocation channels and a histogram showing that discontinuous channels are much more likely to crack. DC: dislocation channel, GB: grain boundary. Images reproduced from [2]

The stress buildup due to dislocation channeling has been shown to act in concert with grain boundary oxidation, known to weaken grain boundaries and promote fracture [5], another key driver of

IASCC [6]. The step height of dislocation channels has also been correlated with IASCC. Austenitic stainless steel (SS) samples with dislocation channel heights measured below a critical value of 300-350 nm did not show IASCC susceptibility in BWR conditions, while samples above that value all experienced IASCC [7]. Jiao et al. explained this critical dislocation height, proportional to the number of glide dislocations in the channel, as the local deformation limit on the dislocation channel to grain boundary interface before the oxide film of the grain boundary ruptures.

1.3 Approach

Researchers at Michigan and others worldwide have spent decades building a mechanistic explanation of IASCC [6], including within the LWRS program. Armed with this explanation (partially described in section 1.2), we have begun efforts aimed at IASCC mitigation. The first phase of mitigation efforts targets stainless steels with microstructural features that may make them resistant to dislocation channeling. Three engineered microstructures were chosen. First, an ODS 304L SS is anticipated to resist dislocation channeling by oxides acting as pinning points, preventing channel formation. Second, an ultrafine-grained (UFG) 304L SS, produced by equal channel angular extrusion, has a high grain boundary density predicted to resist dislocation motion and prevent channeling. Third, an additively manufactured and hot isostatically pressed (AM-HIP) 316L SS has been shown to exhibit broad dislocation channels that result in reduced local strain at grain boundaries (GBs) [8]. These microstructures are shown schematically in Fig. 2.

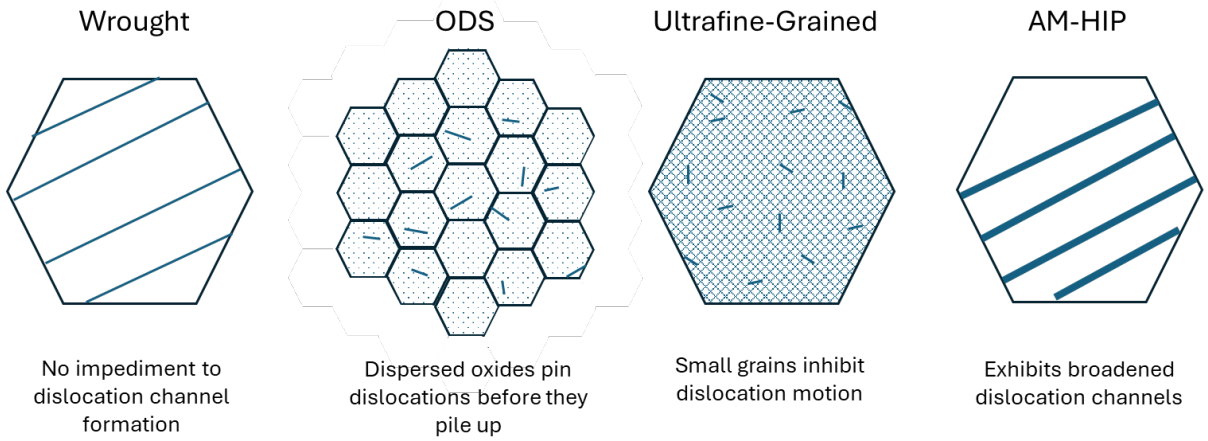

Figure 2: A schematic explanation of the IASCC-resistant microstructures to be examined within this work.

Along with transitioning from understanding IASCC mechanisms to exploring mitigation techniques comes a shift in how experiments must be conducted. While previous experiments used neutron-irradiated samples taken from commercial or test reactors, no such specimens exist for the novel alloys employed by this new mitigation effort. Therefore, samples will be irradiated in-house at the Michigan Ion Beam Laboratory before testing for stress corrosion cracking in LWR conditions. A comparison of neutron and proton irradiated samples is shown in Fig. 3. The purple and the red curves represent stress strain behavior of the neutron and proton irradiated regions, respectively. However, for proton irradiated specimens, the irradiated layer is thin, and the bulk of the sample is non-irradiated and the stress-strain behavior of the whole sample is dominated by the non-irradiated portion of the sample, depicted in light blue. For this reason, efforts in this FY have been aimed at measuring the mechanical properties of the thin irradiated region and modeling the behavior of the coupled irradiated-non-irradiated sample, so we can extract meaningful IASCC data from these samples.

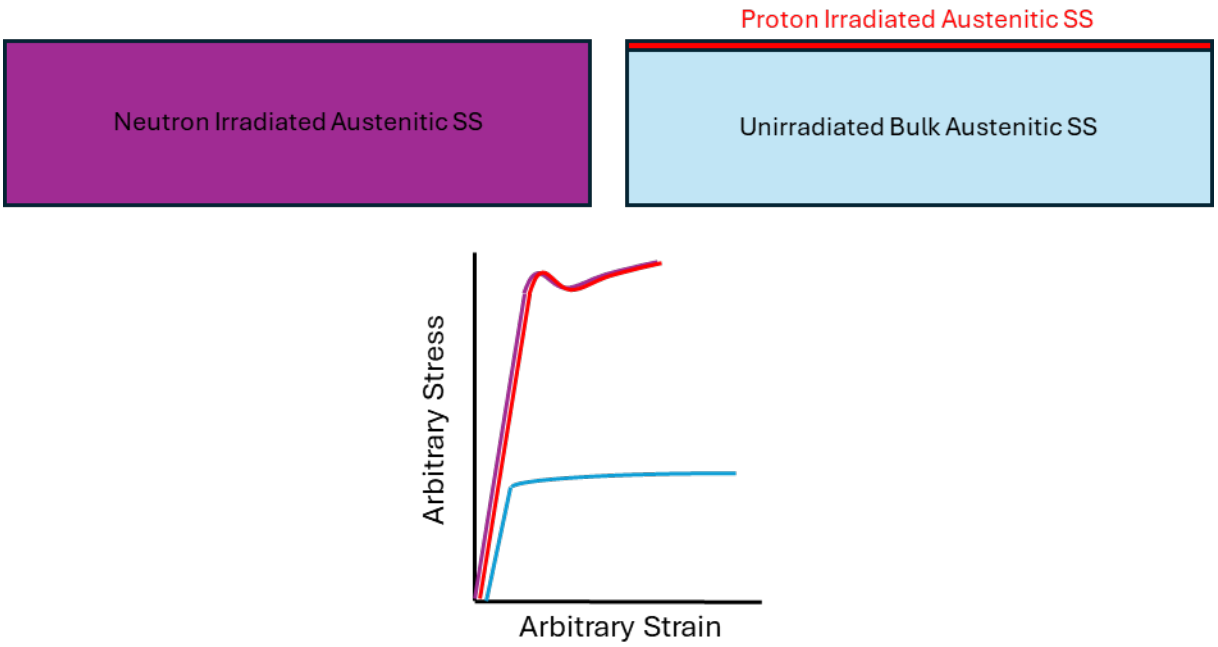

Figure 3: Comparison of stress strain curves for neutron and proton irradiated samples.

A key transition in 4-point bend (4PB) testing is the shift from neutron-irradiated materials to proton-irradiated samples. Proton irradiation presents several advantages for IASCC testing, including faster, more consistent, and cost-effective radiation damage accumulation while significantly reducing radiation exposure to research personnel. The 2 MeV proton irradiation results in radiation damage concentrated within the top 20 μm of the surface layer, sufficient for IASCC initiation studies. Furthermore, IASCC testing of proton-irradiated samples is expedited due to the softer bulk material beneath the irradiated layer, allowing the target surface stress to be achieved more rapidly.

However, a notable challenge in utilizing proton-irradiated 4PB samples for IASCC testing is the complexity of determining the effective surface stress on the proton-irradiated convex bend side. The mechanical behavior of the soft bulk material differs significantly from that of the irradiation-hardened surface layer. The yield strength of the irradiation-hardened layer is approximately four times greater than that of the as-received material, leading to early yielding and permanent plastic deformation in the bulk, even when the surface stress is well below the yield stress. Upon unloading, the entire 4PB sample remains bent, with the entirety of the plastic deformation occurring in the softer bulk. Thus, the surface layer remains elastically bent at loads lower than its yield stress. In contrast, neutron-irradiated samples typically exhibit uniform irradiation hardening throughout the sample, allowing them to behave as a single elastic body below the surface yield stress. As a result, the estimation of surface stress in neutron-irradiated samples was relatively straightforward, with a linear relationship between the applied load and effective stress [9].

After irradiation, the performance of each microstructure will be evaluated using 4PB testing in PWR water at 320 °C. Since proton irradiation cannot uniformly irradiate the samples' thickness, an finite element analysis (FEA) model (described in section 2.5) is employed to interpret the results of 4PB testing.

In this work, we discuss recent progress toward our goal of measuring IASCC in alloys with engineered microstructures designed to resist IASCC. We will describe proton irradiation experiments, and preparation for novel 4-point bend IASCC testing on proton irradiated samples, made necessary by using these new alloys.

2. Experiment

2.1 Sample Preparation

2.1.1 Sample History

Samples were sourced from researchers at the University of Nebraska–Lincoln, researchers at Purdue University, and the Yuen Chang Stainless Steel Corporation. The ODS 304L SS provided by the University of Nebraska was fabricated by spark plasma sintering and is described in [10]. The UFG 304L SS was manufactured at Taxes A&M University by equal channel angular pressing to reduce grain size to 0.1 μm [11]. The AM-HIP 316L SS was provided by Dr. Xiaoyuan Lou at Purdue, and was manufactured from commercial powder using laser powder bed fusion and processed using a hot isostatic press [8]. The wrought (WR) 304L was purchased from the Yuen Chang Stainless Steel Corporation, where it was cold rolled. The compositions of each material are given in Table 1, as reported by the providing institutions.

Table 1: Composition of AM-HIP, ODS, UFG, and WR samples.

Element (wt %)	Fe	Cr	Ni	Si	Mn	Mo	Co	C	N	Y_2O_3	Ti	W
AM-HIP 316L SS	Bal.	17	10	1	2	2.5	-	0.03	0.1	-	-	-
ODS 304L	Bal.	18	8.5	-	-	-	-	-	-	0.35	0.5	2
UFG 304L	Bal.	18.19	8.04	0.3	1.68	0.12	0.16	0.02	0.08	-	-	-
WR 304L	Bal.	18.09	8.01	0.41	1.43	0.03	-	0.025	0.072	-	-	-

2.1.2 Four-Point Bend Test Geometry

For the 4PB test (described also in section 2.4.2), samples with dimensions of 5 x 3.5 x 2 mm were prepared from the as-received material plates or blocks using electrical discharge machining technique. The 4PB samples from the WR 304L plate were machined such that the longitudinal axis of the sample was aligned with the rolling direction, while the transverse axis corresponded to the long transverse direction (see Fig. 4). Both sides of the short transverse direction of the samples were ground and polished to achieve a final thickness between 0.8 and 0.9 mm. For all samples, the side intended for irradiation was finely polished. The WR 304L sample was electropolished in a 10% perchloric acid 90% methanol solution at –45 °C. However, electropolishing did not produce the desired surface finish for other samples, which were instead vibratory polished using 0.04 μm colloidal silica as a final step. Due to its combined chemical-mechanical effects, vibratory polishing has been reported to yield a damage-free surface layer [12].

Guide bars of 304L steel were ground to the final thickness of 0.9 mm and polished on the short transverse direction to 1200 grit. These bars, cut by electrical discharge machining to 12 x 2 x 1.5 mm before final grinding, provide surfaces on which thermocouples could be welded to monitor the samples between them.

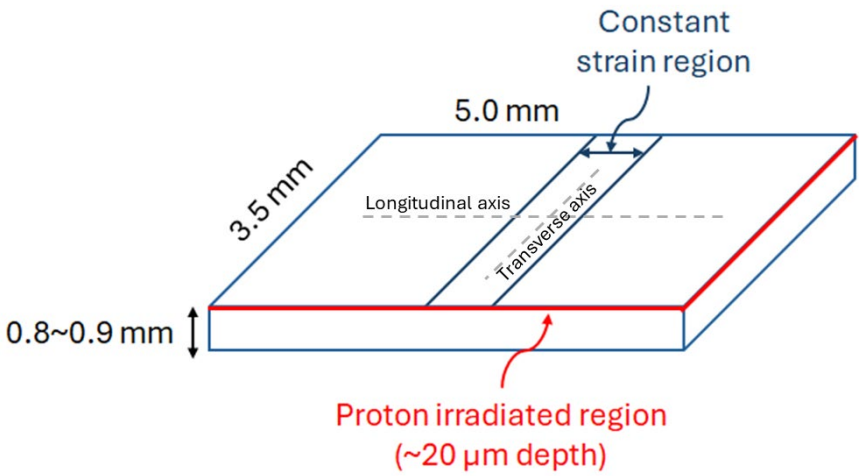

Figure 4: Schematic of 4PB sample geometry and orientation.

2.2 Irradiation

2.2.1 SRIM

Stopping and range of ions in matter (SRIM) calculations were performed for 304L and 316L steels using the quick Kinchin-Pease model, yielding similar damage profiles. The ODS dpa profile is shown in Fig. 5. The incident energy was 2 MeV with 100,000 simulated ions. The target dose of 5 dpa was selected at 13 µm below the surface, consistent with other IASCC experiments and within the linear damage region in the profile.

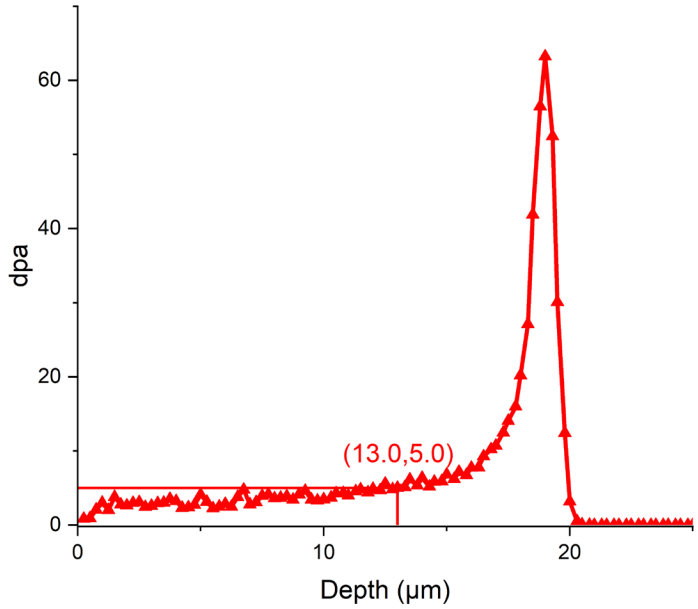

Figure 5: SRIM profile of ODS 304L.

2.2.2 Stage Preparation

Two 4PB samples of ODS 304L, AM-HIP 316L, and WR 304L stainless steels were prepared for proton irradiation, while the UFG 304L samples are planned for following irradiations. The samples were mounted onto a copper stage that was cleaned and flattened with a rasp before applying an even layer of silver paste. Each sample was placed on the silver paste and pressed firmly to ensure proper adhesion. The stage was heated to 100 °C to harden the paste. Thermocouples were spot-welded to the guide bars, and hold-down bars were tightened to secure the guide bars in place, ensuring stable positioning of the samples during the experiment. The mounted stage is shown in Fig. 6.

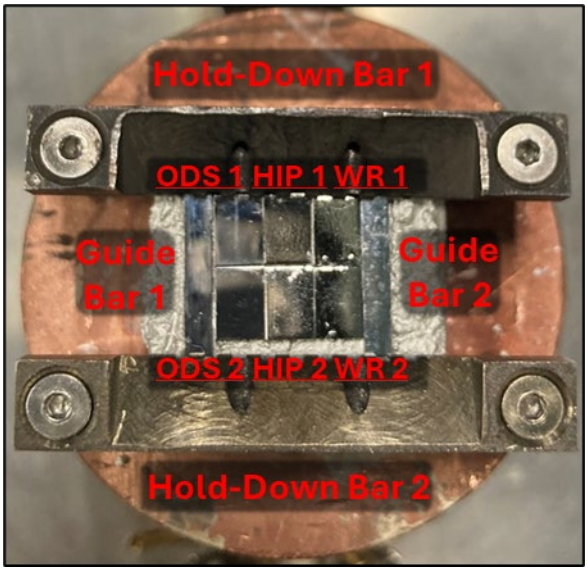

Figure 6: Copper stage for irradiation, mounted with 6 samples, guide bars, and hold-down bars

The stage was mounted into a chamber at the end of a beamline at the Michigan Ion Beam Laboratory and pumped down to a vacuum level of 10^{-7} torr. Initially, the stage was heated to 360 °C, as monitored by thermocouples, to facilitate the calibration of the infrared (IR) camera. A centered stationary beam with a Gaussian profile was used, balanced across apertures to ensure a centered beam and complete irradiation across the sample surface.

2.3 Indentation

One challenge with the switch from neutron irradiation to proton irradiation is measuring the high-temperature mechanical properties of the irradiated specimens. The thin irradiated layers, around 20 µm, cannot be characterized by traditional methods, and no literature data exists for the high-temperature yield strength of the materials with novel microstructures, let alone their yield strengths at high temperatures after irradiation. Despite the lack of data, these are key inputs for the FEA model and are necessary for conducting proper 4PB tests (described in section 2.5.1).

IASCC tests will be conducted at 320 °C in PWR water, necessitating material property data at this temperature for a more accurate simulation of sample bending. First, to determine the mechanical properties of the bulk layer at high temperature, SSJ2 specimens will be prepared from the as-received materials and strained in 320 °C argon. We anticipate gathering this data during the next FY. However, obtaining mechanical property data for the irradiation-hardened surface layer at 320 °C is a more difficult challenge. The limited sampling volume precludes the use of conventional macroscale testing techniques, necessitating microscale mechanical testing methods.

Vickers hardness measurements at 25 gf are an applicable technique to evaluate the mechanical response of the irradiation-hardened layer, with a plastic deformation depth of less than 2 µm, well within

the proton irradiation range [13]. Previous studies have reported a linear correlation between the yield strength of irradiated austenitic stainless steels and Vickers hardness data, demonstrating excellent agreement, independent of material composition or test temperature [14]. While this correlation can be used to derive room-temperature mechanical properties from Vickers hardness, it cannot be directly applied to estimate the yield strength at 320 °C due to the lack of facilities for high-temperature Vickers hardness measurements.

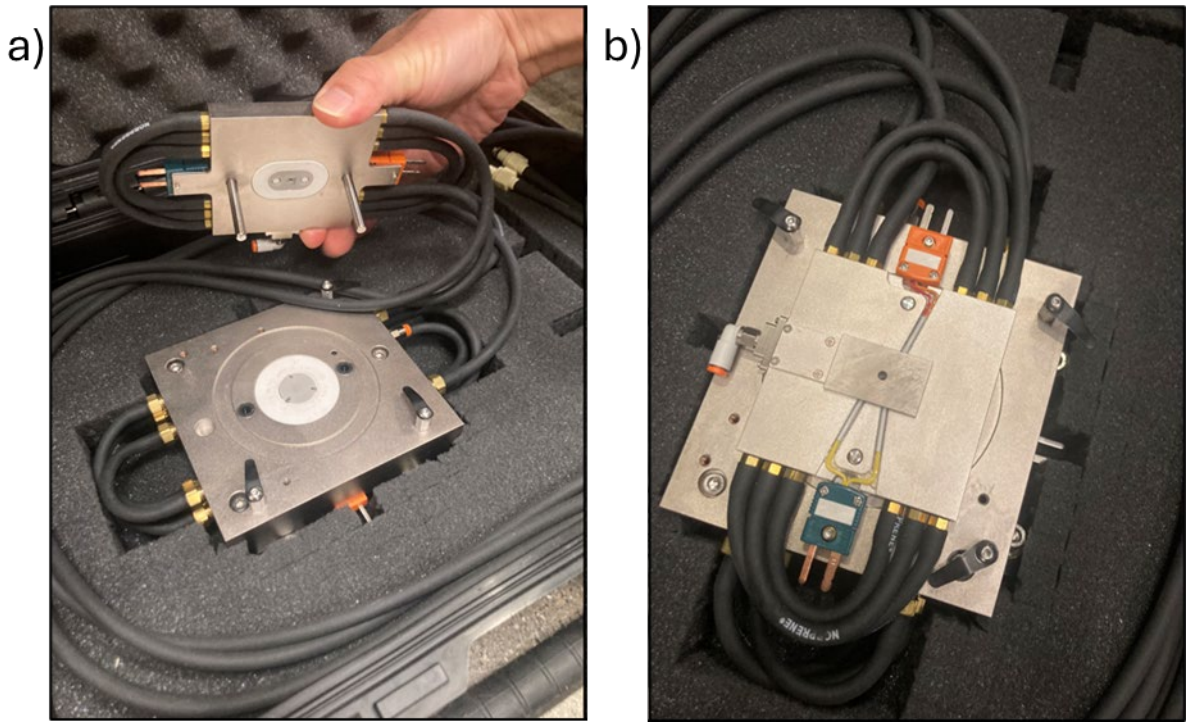

Figure 7: xSol Stage for the Hysitron Triboindenter, open (a) and closed (b).

One method to obtain the high-temperature yield strength of the proton irradiated regions is through high-temperature indentation. For this work, a Hysitron 950 Triboindenter was used, with a newly purchased high-temperature stage, capable of reaching 320 °C with argon gas for shielding, as shown in Fig. 7. The Hysitron indenter tip uses the Berkovich geometry, contrasted to the Vickers indenter in Fig. 8. Both indenters produce similar results due to their connected geometry, shown by values such as projected area, volume-depth relation, and equivalent cone angle shown in Table 2.

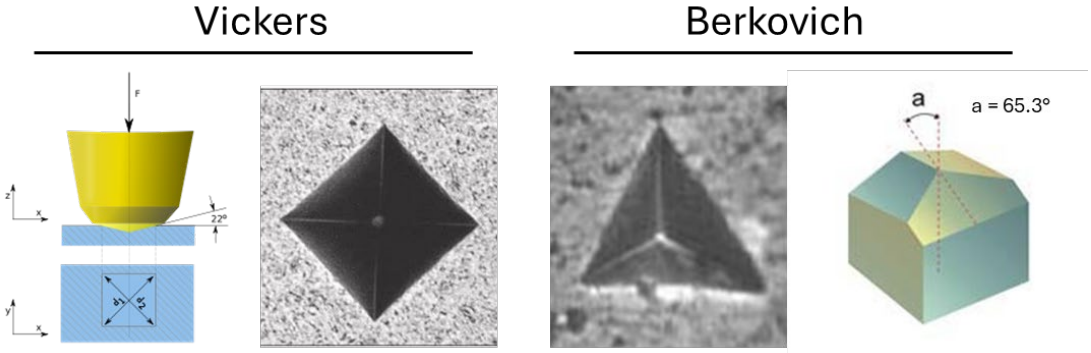

Figure 8: Comparison of Vickers and Berkovich indentation probes.

Table 2: Summary of nominal geometric relationships for several indenters used in instrumented indentation testing. Table reproduced from [15].

Parameter	Vickers	Berkovich	Cube-corner	Cone (angle ψ)	Sphere (radius R)
Centerline-to-face angle, α	68°	65.3°	35.2644°	…	…
Area (projected), $A(d)$	24.504 d^2	24.56 d^2	2.5981 d^2	πa^2	πa^2
Volume-depth relation, $V(d)$	8.1681 d^3	8.1873 d^3	0.8657 d^3	…	…
Projected area/face area, A/A_f	0.927	0.908	0.5774	…	…
Equivalent cone angle, ψ	70.2996°	70.32°	42.28°	ψ	…
Contact radius, a	…	…	…	$d \tan \psi$	$(2Rd - d^2)^{1/2}$

2.4 IASCC Testing

2.4.1 Irradiated Material System

The Irradiated Materials Testing Laboratory (IMTL) at the University of Michigan is equipped with multiple autoclave systems designed for testing irradiated materials in aqueous environments. The 4PB IASCC tests for the scoped work will be conducted in parallel using the IM2 and IM3/IM5 systems. The IASCC tests will be performed in a simulated PWR water chemistry environment at 320 °C and 2000 psi. The pictures and schematic of the IM2 test loop are shown in Figs. 9 & 10.

a) b)

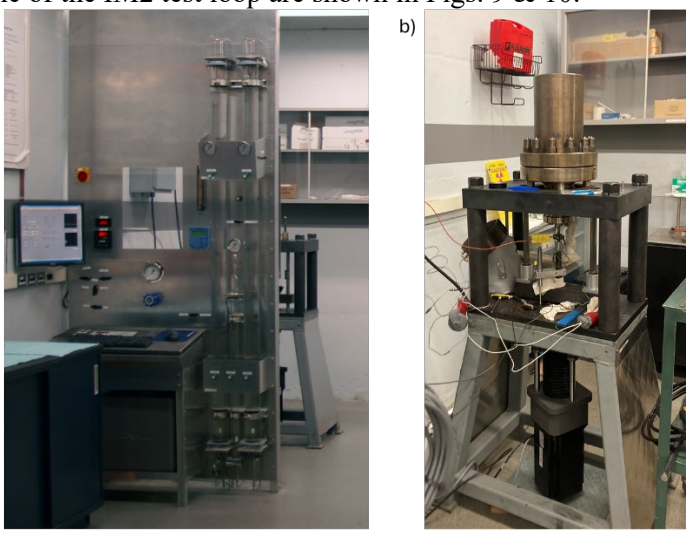

Figure 9: a) IM2 front panel with main and makeup columns and b) IM2 autoclave and motor system.

IM2

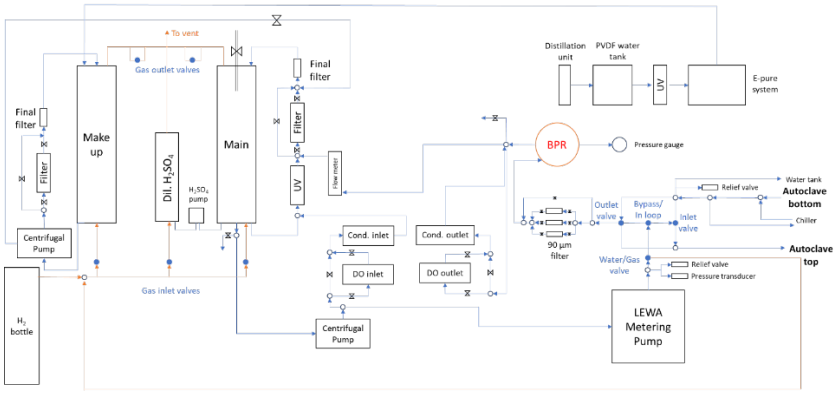

Figure 10: Irradiated Materials System 2 (IM2) diagram.

During the experiments, the main column will be filled with PWR water with 1000 ppm B (as H_3BO_3) and 2 ppm Li (as LiOH). This water chemistry corresponds to a pH of 6.5 and conductivity of 21.5 µS/cm, which will be monitored throughout the test. A hydrogen overpressure will be maintained in the main column to achieve a dissolved hydrogen concentration of 35 cc/kg. The main column water will be continuously circulated through an ion exchange filter saturated with borate and Li cations, which will be used to remove ionic impurities. A custom LabView code will monitor, control, and record all experimental parameters during testing.

2.4.2 Four-Point Bend Fixture

The 4PB test was recently developed for IASCC initiation studies, particularly suited for neutron-irradiated samples where limited material volume and availability are common [9], [16], [17], [18], [19]. This test generates an area (0.5 x 3.5 mm) of nearly uniaxial tensile stress and strain in the central region of the sample (Fig. 4), promoting multiple crack initiation sites within a single specimen. The primary objective is to determine the fraction of irradiated yield strength at which the material becomes susceptible to IASCC initiation. To achieve this, interrupted loading steps will be conducted, whereby the sample is sealed in the PWR environment and incrementally loaded below the irradiated yield stress, followed by periodic unloading for crack inspection using scanning electron microscopy (SEM).
The schematic diagram of the 4PB test setup is shown in Fig. 11. Two fixture assemblies were fabricated to allow parallel testing in two autoclave systems (IM2 and IM3/IM5). The setup comprises an upper-loading punch with two closely spaced indents and a lower sample support. The sample is carefully positioned at the center of the fixture using non-metallic tweezers, ensuring that the proton-irradiated surface, which is susceptible to IASCC, faces downward. Centering pins are used to position the sample precisely. A photograph is taken to verify that the indents are aligned with the center of the sample and to ensure consistent placement during subsequent incremental loading. The upper-loading punch contacts the opposite side of the sample and moves downward to apply the load, causing the sample to bend convexly on the downward-facing irradiated surface. The 4PB tests will start with loading up to 40% of the irradiated yield strength, followed by 10% load increments until crack initiation is observed. Most fixture components were fabricated from 316 SS material, while the critical load-transferring parts, including the upper-loading punch and sample support, were made from solution-annealed Inconel 718. The Inconel 718 components were age-treated at 720°C for 8 hours, followed by 620°C for 10 hours in an argon environment. As a result of the aging treatment, the hardness of these components increased from 220 HV0.5 to 524 HV0.5.

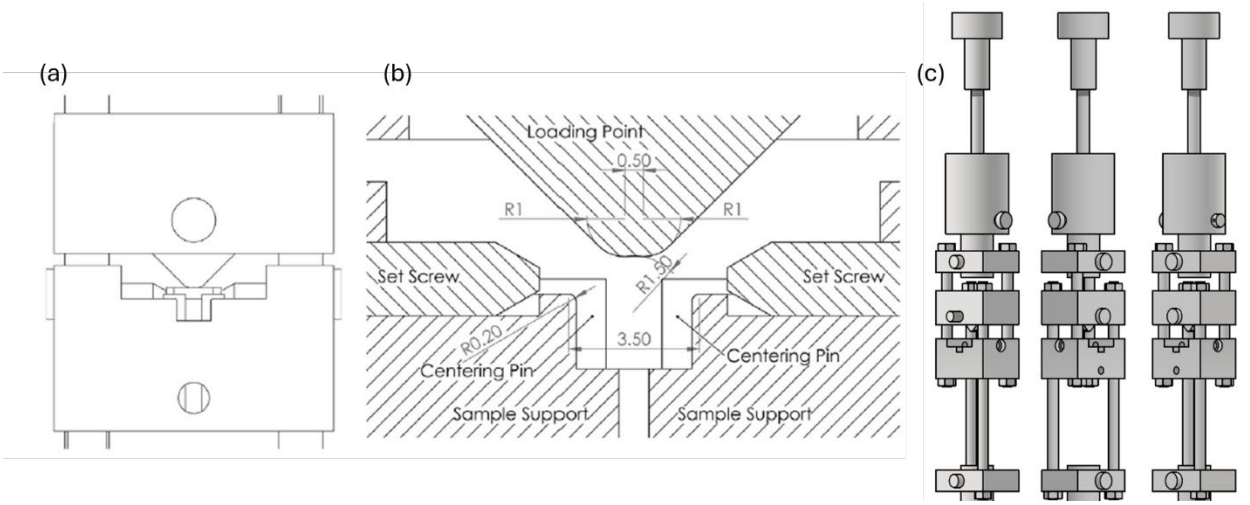

Figure 11: (a) Schematic, (b) cross-section view of the 4PB loading fixture [9] and (c) computer-aided design (CAD) drawing of the fully assembled loading fixture.

2.4.3 IASCC Experimental Setup

The 4PB sample will be carefully loaded into the test fixture and aligned to ensure consistent positioning between loading steps. The autoclave will be sealed, filled with PWR water, pressurized to 2000 psi, and heated to 320 °C. Once the system stabilizes under the test conditions, the test fixture's pull rod will be connected to a crosshead driven by a stepping motor. The motor will be programmed to lower the crosshead, dynamically straining the 4PB sample surface at a strain rate of 4×10^{-8} /s. The initial step involves loading from 0% to 40% of the irradiated yield strength of the sample, after which the sample will be unloaded once the target stress is reached. The load corresponding to the target surface stress value will be determined by the FEA simulation (described in section 2.5.1).

After the autoclave is cooled to room temperature, the sample will be removed for crack examination. Examination will be confined to a uniformly strained central region measuring 0.5 × 3.5 mm, previously identified by indent marks on the irradiated side of the sample. A JEOL JSM-6480 scanning electron microscope (SEM) in backscattered electron (BSE) mode will inspect the sample for cracks at 1000X magnification. If no cracks are detected, the sample will be reloaded at an additional 10% of the irradiated yield strength under the same experimental conditions. This process will be repeated until cracking is observed. The location of observed cracks will be documented to correlate with previous loading steps and to identify any microstructural features preceding crack formation. Detailed statistical analysis will be performed on the cracking behavior, and the fraction of irradiated yield strength at which cracking occurs will be used to compare IASCC susceptibility between stainless steels with novel microstructures. High-resolution transmission electron microscopy (TEM) will be conducted at the crack tip regions to investigate the grain boundary oxide formation, microstructural characteristics, and factors contributing to IASCC initiation.

2.5 Modeling

2.5.1 Finite Element Analysis

IASCC initiation occurs well below the irradiated yield stress [6], making it critical to establish the stress levels at which cracking initiates for quantifiable comparisons of material susceptibility. The use of proton-irradiated samples instead of neutron-irradiated samples presents a challenge due to the inhomogeneity of the proton-irradiated samples. The region of interest is a thin irradiated layer around 20 μm thick, while the bulk of the sample is unirradiated. Therefore, while we are interested in applying a particular strain to the irradiated region, we must recognize that the unirradiated bulk dominates the mechanical response of the sample. Due to the distinct mechanical behaviors of the two layers in proton-

irradiated 4PB samples, a customized finite element analysis (FEA) simulation is necessary to estimate the effective surface stress. The objective of the simulation is to determine the mechanical load required to achieve the target surface stress, starting at 40% of the irradiated yield strength, with subsequent 10% increments. For accurate surface stress estimation, it is essential to provide the FEA program with material properties for both layers, including yield strength, modulus of elasticity, strain-hardening coefficient, friction coefficient, Poisson's ratio, and density. The FEA code is currently being developed using the ANSYS platform and is undergoing optimization to improve simulation efficiency. The code will be validated with experimental results.

3. Results

3.1 Irradiation

The irradiation results of the ODS 304, AM-HIP 316, and WR 304 samples are shown in Table 3. The temperature and pressure were steady throughout the experiment. The standard deviation for the temperature is slightly larger than expected because specimen WR 2 was an outlier. The stage current was steady at around 23 µA throughout the experiment. The proton source experienced some instability from arcing during the week-long irradiation, leading to the six drops in current shown in Fig. 12a. Each time the stage briefly lost current, the temperature immediately dropped. The drop in temperature ensured that the defects created by irradiation were not annealed, and the irradiation could resume when the current was restored.

Table 3: Irradiation record.

	Target	Achieved
Damage Level (dpa)	5	5
Damage Rate (dpa/s)	8.42 x 10^{-6}	8.34 x 10^{-6}
Temperature (°C ± 2σ)	360	359.3 ± 8.8
Chamber Pressure (torr)	8 x 10^{-8}	9.95 x10^{-8}

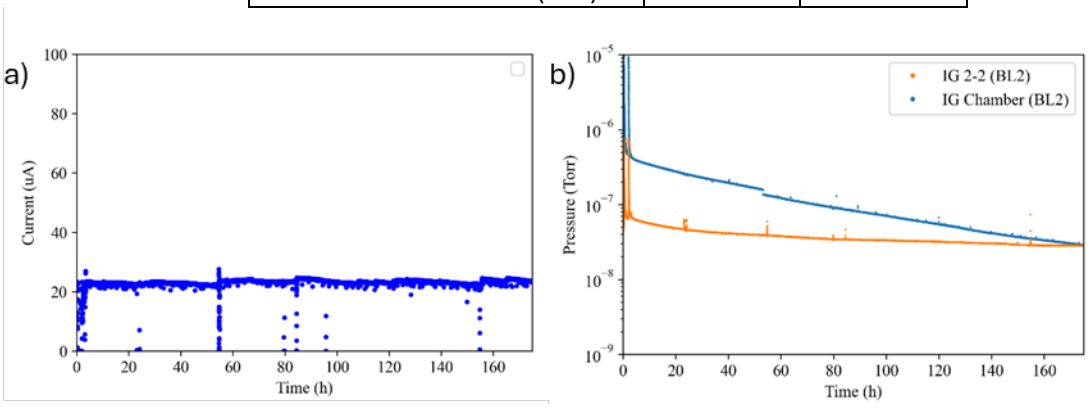

Figure 12: a) Stage current of proton irradiation and b) chamber and beamline pressures during the irradiation for 167 hours at 360°C to 5 dpa at a damage rate of 8.34 x 10^{-6} dpa/s

Unexpectedly, the ODS samples exhibited a visible oxide after irradiation despite the low chamber pressure of 10^{-7} Torr. Under SEM, the surface oxide was shown to form preferentially along grain boundaries. Future EDS will identify the composition of the oxide.

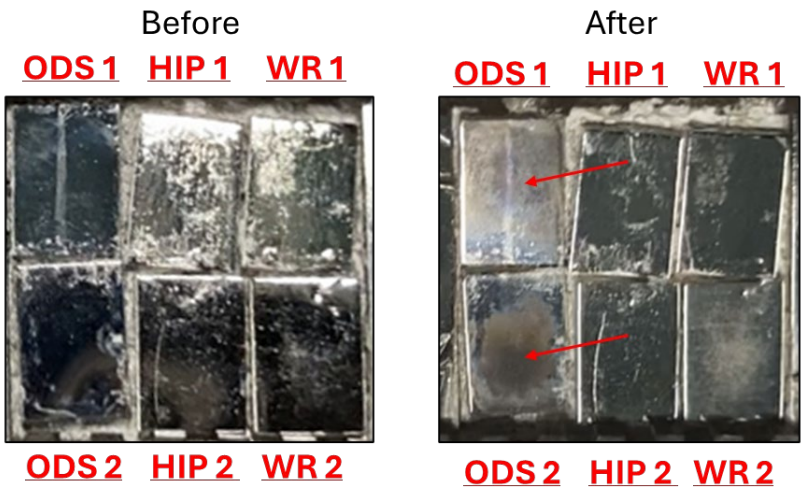

Figure 13: Photographs of the sample surfaces before and after irradiation for 167 hours at 360°C to 5 dpa at a damage rate of 8.34 x 10^{-6} dpa/s

The bottom right sample in Fig. 13 (WR 2) had a temperature 40 °C higher than the rest of the samples due to the silver paste buildup on one end. As samples were affixed to the stage, each one was pressed individually. If a sample was not securely held once the paste dried, it was removed, and additional paste was applied before repositioning. The buildup of silver paste shown in Fig. 14 on the right end of WR 2 elevated the sample slightly, reducing thermal contact between the sample and the stage. This reduced contact hindered the dissipation of heat generated by irradiation, preventing effective heat transfer to the cooled copper stage. To address this issue in future tests, we will apply a thinner layer of silver paste, and any samples removed between drying intervals will be thoroughly cleaned before reapplication.

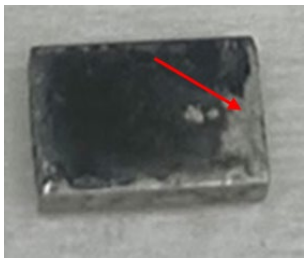

Figure 14: WR 2 sample after irradiation with protons for 167 hours at 360°C to 5 dpa at a damage rate of 8.34 x 10^{-6} dpa/s showing silver paste buildup (arrowed).

3.2 Indentation Results

Hardness measurements were taken on the irradiated specimens at room temperature as a baseline using 250 mN force on the indenter tip. Indents were made in a 5 by 6 array spaced 50 µm apart. This spacing was chosen to be greater than 5x the diameter of the indent, which mitigates the potential interaction between indents. A load of 250 mN for Berkovich indentation was selected to mimic 25 gf indents performed on a Vickers machine at the University of Michigan. A load of 25 gf is standard for proton-irradiated stainless steel to achieve a penetration depth of around 2 µm into the sample surface. The results in Fig. 15 for the irradiated samples varied greatly, indicating that an improvement in methods is needed to obtain reliable indentation data. For wrought austenitic stainless steels irradiated to 5 dpa, the expected hardness values range from 1 to 4 GPa [14]. The measured hardness of specimen WR1 had an average of 8 GPa, indicating that further calibration must be done. Fig. 16 maps the hardness of the ODS 2 sample surface, which shows a clear trend of higher hardness to the top right of the sample. One source

of error could be the method used for bonding samples to the stage. The second source of error could be surface defects such as oxidation from the irradiation.

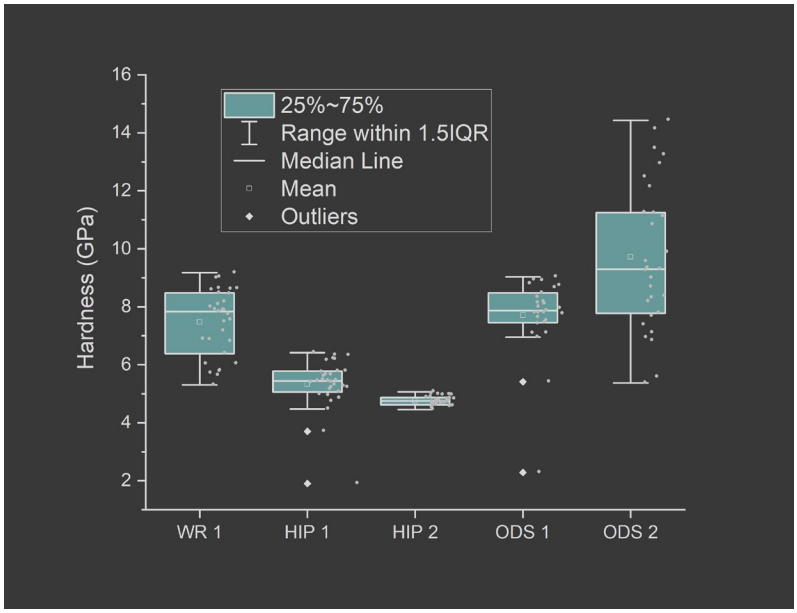

Figure 15: Indentation results by sample, all irradiated with protons for 167 hours at 360°C to 5 dpa at a damage rate of 8.34 x 10^{-6} dpa/s

The first source of error (bonding to the stage) will be mitigated in the future by utilizing magnetic mounting discs that will be superglued hours before the indentation session and mounted magnetically to the stage. The second source will be mitigated by applying a gentle polish to the surface of the irradiated samples to remove oxides.

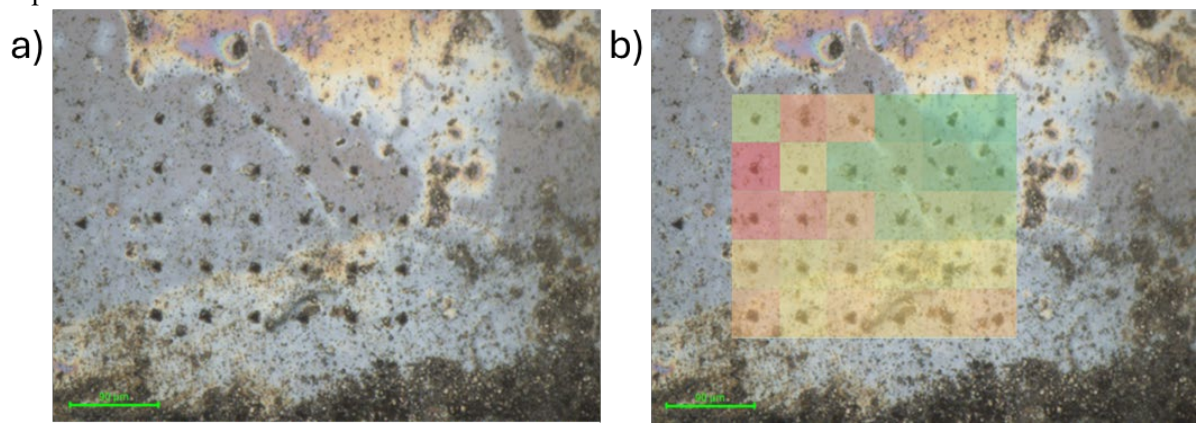

Figure 16: Hardness map of ODS 2 sample, with the map overlay ranging from red (2.8 GPa) to green (14.4 GPa).

3.3 TEM Characterization

A TEM specimen was prepared from the ODS sample using the focused ion beam (FIB) lift-out technique to investigate from the surface to a depth of 5 µm. Due to surface oxide along GBs from irradiation, electron backscatter diffraction (EBSD) analysis of the surface was limited to large grains. The lift-out was taken from these large grains and does not represent the typical microstructure shown beneath the outlined grain in Fig. 18.

The center grain was indexed on the z = [011] zone axis. The center grain exhibits twinning. Images taken using the rel-rod method revealed dislocation loops and what appear to be either cavities or oxide particles, shown in Fig. 17. Further imaging and analysis will be conducted to confirm.

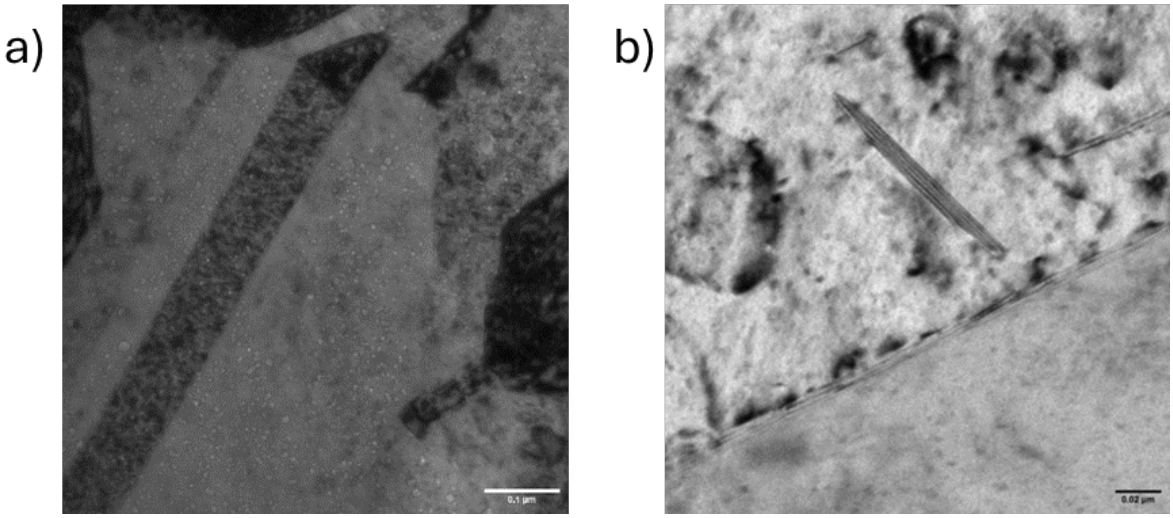

Figure 17: Bright field images of a) cavities or oxide particles and b) dislocation loops.

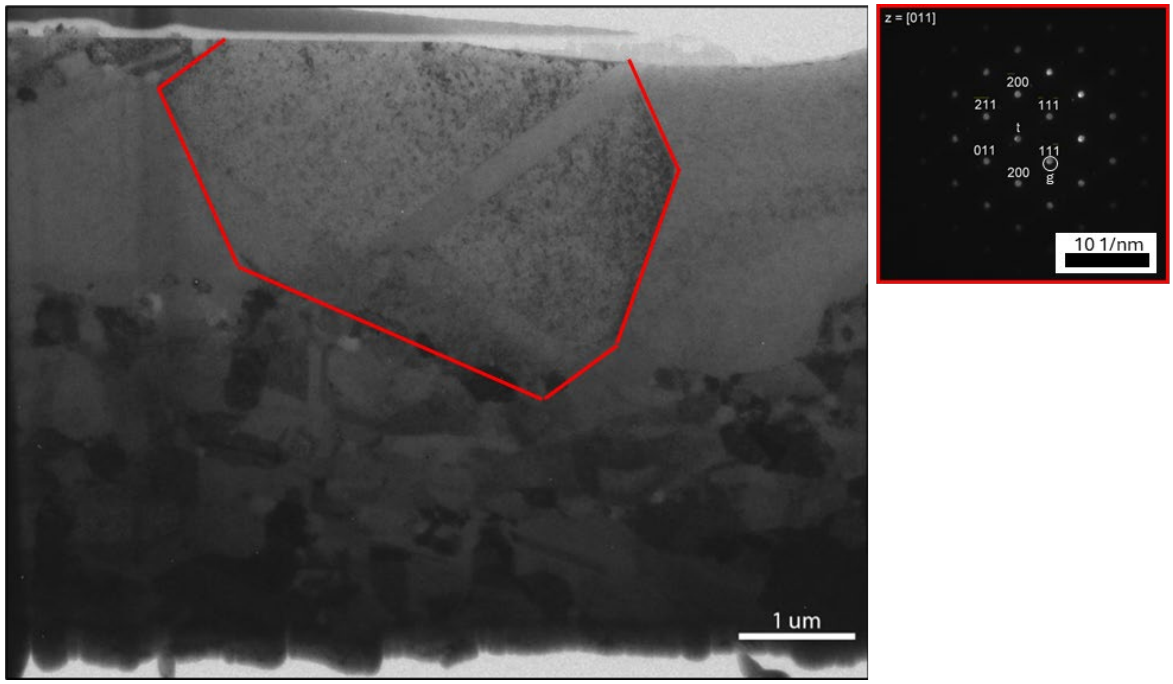

Figure 18: Bright field map of FIB lift-out taken from ODS surface. The diffraction pattern for the indexed grain (outlined) is shown to the right.

A dislocation loop density of 3.3 x 10^{14} m^{-2} was measured in the indexed grain shown in Fig. 18. Table 4 compares other austenitic stainless steels from the literature to this measurement of dislocation density. Because this lift-out is not representative of the entire microstructure, future measurements of dislocation density in another lift-out will be taken to compare with the unirradiated and irradiated WR, AM-HIP, and UFG microstructures.

Table 4: Comparison of dislocation density between austenitic stainless steels.

Material	Dose, dpa	Temperature, °C	Dislocation Density, 10^{14} m^{-2}
ODS 2	5	360	3.3
ODS 304 [20]	0	25	3
AM 316L [21]	2	450	5.2

4. Conclusions

Work has begun on transitioning from understanding IASCC mechanisms to exploring novel microstructures for mitigating IASCC. We have shifted from IASCC testing on commercial alloys irradiated in commercial or test reactors to IASCC testing on alloys with novel microstructures that we irradiated with protons in-house. This shift has necessitated qualifying new procedures for IASCC testing on proton irradiated samples, including new methods for modeling their mechanical behavior and experimentally measuring the mechanical properties of the irradiated regions. We have reported initial progress on the proton irradiation of ODS and AM-HIP stainless steels and discussed plans for measuring the high-temperature yield strength of the proton irradiated regions of the samples to enable effective 4PB testing. Future work will include IASCC testing results on these alloys and a comparative analysis with wrought stainless steels to provide initial data on the effectiveness of these engineered microstructures at resisting IASCC.

5. References

[1] N. Hashimoto, S. J. Zinkle, A. F. Rowcliffe, J. P. Robertson, and S. Jitsukawa, "Deformation mechanisms in 316 stainless steel irradiated at 60°C and 330°C," *J. Nucl. Mater.*, vol. 283–287, pp. 528–534, Dec. 2000, doi: 10.1016/S0022-3115(00)00087-8.

[2] M. D. McMurtrey, G. S. Was, L. Patrick, and D. Farkas, "Relationship between localized strain and irradiation assisted stress corrosion cracking in an austenitic alloy," *Mater. Sci. Eng. A*, vol. 528, no. 10, pp. 3730–3740, Apr. 2011, doi: 10.1016/j.msea.2011.01.073.

[3] D. C. Johnson, B. Kuhr, D. Farkas, and G. S. Was, "Quantitative linkage between the stress at dislocation channel – Grain boundary interaction sites and irradiation assisted stress corrosion crack initiation," *Acta Mater.*, vol. 170, pp. 166–175, May 2019, doi: 10.1016/j.actamat.2019.02.032.

[4] B. Kuhr, D. Farkas, I. M. Robertson, D. Johnson, and G. Was, "Stress Localization Resulting from Grain Boundary Dislocation Interactions in Relaxed and Defective Grain Boundaries," *Metall. Mater. Trans. A*, vol. 51, no. 2, pp. 667–683, Feb. 2020, doi: 10.1007/s11661-019-05534-0.

[5] H. Dugdale, D. E. J. Armstrong, E. Tarleton, S. G. Roberts, and S. Lozano-Perez, "How oxidized grain boundaries fail," *Acta Mater.*, vol. 61, no. 13, pp. 4707–4713, Aug. 2013, doi: 10.1016/j.actamat.2013.05.012.

[6] G. S. Was *et al.*, "How irradiation promotes intergranular stress corrosion crack initiation," *Prog. Mater. Sci.*, vol. 143, p. 101255, Jun. 2024, doi: 10.1016/j.pmatsci.2024.101255.

[7] Z. Jiao and G. S. Was, "Impact of localized deformation on IASCC in austenitic stainless steels," *J. Nucl. Mater.*, vol. 408, no. 3, pp. 246–256, Jan. 2011, doi: 10.1016/j.jnucmat.2010.10.087.

[8] J. Yang *et al.*, "Dislocation channel broadening–A new mechanism to improve irradiation-assisted stress corrosion cracking resistance of additively manufactured 316 L stainless steel," *Acta Mater.*, vol. 266, p. 119650, Mar. 2024, doi: 10.1016/j.actamat.2024.119650.

[9] K. J. Stephenson and G. S. Was, "The role of dislocation channeling in IASCC initiation of neutron irradiated stainless steel," *J. Nucl. Mater.*, vol. 481, pp. 214–225, Dec. 2016, doi: 10.1016/j.jnucmat.2016.09.001.

[10] X. Yan *et al.*, "Fabrication of ODS Austenitic Steels and CoCrFeNi High-Entropy Alloys by Spark Plasma Sintering for Nuclear Energy Applications," *JOM*, vol. 71, no. 8, pp. 2856–2867, Aug. 2019, doi: 10.1007/s11837-019-03531-7.

[11] C. Sun *et al.*, "Superior radiation-resistant nanoengineered austenitic 304L stainless steel for applications in extreme radiation environments," *Sci. Rep.*, vol. 5, no. 1, p. 7801, Jan. 2015, doi: 10.1038/srep07801.

[12] "Mechanical Grinding and Polishing", doi: https://doi.org/10.31399/asm.hb.v09.9781627081771.

[13] L. Hawkins *et al.*, "The effect of secondary phases on microstructure and irradiation damage in an as-built additively manufactured 316 L stainless steel with a hafnium compositional gradient," *J. Nucl. Mater.*, vol. 587, p. 154708, Dec. 2023, doi: 10.1016/j.jnucmat.2023.154708.

[14] J. T. Busby, M. C. Hash, and G. S. Was, "The relationship between hardness and yield stress in irradiated austenitic and ferritic steels," *J. Nucl. Mater.*, vol. 336, no. 2, pp. 267–278, Feb. 2005, doi: 10.1016/j.jnucmat.2004.09.024.

[15] H. Kuhn and D. Medlin, Eds., “Instrumented Indentation Testing,” in *Mechanical Testing and Evaluation*, ASM International, 2000, pp. 232–243. doi: 10.31399/asm.hb.v08.a0003273.
[16] D. Du, K. Sun, and G. S. Was, “IASCC of neutron irradiated 316 stainless steel to 125 dpa,” *Mater. Charact.*, vol. 173, p. 110897, Mar. 2021, doi: 10.1016/j.matchar.2021.110897.
[17] K. Chen, M. R. Ickes, M. A. Burke, and G. S. Was, “The effect of potassium hydroxide primary water chemistry on the IASCC behavior of 304 stainless steel,” *J. Nucl. Mater.*, vol. 558, p. 153323, Jan. 2022, doi: 10.1016/j.jnucmat.2021.153323.
[18] S. Swaminathan, K. Sun, and G. S. Was, “Decoupling the roles of grain boundary oxidation and stress in IASCC of neutron-irradiated 304L stainless steel,” *J. Nucl. Mater.*, vol. 585, p. 154604, Nov. 2023, doi: 10.1016/j.jnucmat.2023.154604.
[19] A. S. Sinjlawi, L. Dong, M. Ickes, K. Sun, and G. S. Was, “Irradiation assisted stress corrosion cracking of 347 stainless steel in simulated PWR primary water containing lithium hydroxide or potassium hydroxide,” *J. Nucl. Mater.*, vol. 586, p. 154676, Dec. 2023, doi: 10.1016/j.jnucmat.2023.154676.
[20] Y. Miao, “Advanced characterizations of austenitic oxide dispersion-strengthened (ODS) steels for high-temperature reactor applications,” text, University of Illinois at Urbana-Champaign, 2015. Accessed: Sep. 19, 2024. [Online]. Available: https://hdl.handle.net/2142/88013
[21] S. Li, J. Hu, W.-Y. Chen, J. Yu, M. Li, and Y. Wang, “Evolution of cellular dislocation structures and defects in additively manufactured austenitic stainless steel under ion irradiation,” *Scr. Mater.*, vol. 178, pp. 245–250, Mar. 2020, doi: 10.1016/j.scriptamat.2019.11.036.